Downstream Suppression of Baroclinic Waves

LINA BOLJKA,[a] DAVID W. J. THOMPSON,[a] AND YING LI[a]

[a] *Department of Atmospheric Science, Colorado State University, Fort Collins, Colorado*

(Manuscript received 24 June 2020, in final form 12 November 2020)

ABSTRACT: Baroclinic waves drive both regional variations in weather and large-scale variability in the extratropical general circulation. They generally do not exist in isolation, but rather often form into coherent wave packets that propagate to the east via a mechanism called downstream development. Downstream development has been widely documented and explored. Here we document a novel but also key aspect of baroclinic waves: the *downstream suppression* of baroclinic activity that occurs in the wake of eastward propagating disturbances. Downstream suppression is apparent not only in the Southern Hemisphere storm track as shown in previous work, but also in the North Pacific and North Atlantic storm tracks. It plays an essential role in driving subseasonal periodicity in extratropical eddy activity in both hemispheres, and gives rise to the observed quiescence of the North Atlantic storm track 1–2 weeks following pronounced eddy activity in the North Pacific sector. It is argued that downstream suppression results from the anomalously low baroclinicity that arises as eastward propagating wave packets convert potential to kinetic energy. In contrast to baroclinic wave packets, which propagate to the east at roughly the group velocity in the upper troposphere, the suppression of baroclinic activity propagates eastward at a slower rate that is comparable to that of the lower to midtropospheric flow. The results have implications for understanding subseasonal variability in the extratropical troposphere of both hemispheres.

KEYWORDS: Atmosphere; Baroclinic flows; Dynamics; Waves, atmospheric; Intraseasonal variability

1. Introduction

Baroclinic instability is a predominant source of extratropical atmospheric variability (Charney 1947; Eady 1949). It gives rise to baroclinic waves, which drive not only day-to-day variations in weather throughout the midlatitudes (Hoskins and James 2014), but also variations in the large-scale general circulation through their fluxes of heat, momentum, and potential vorticity (Andrews and McIntyre 1976; Blackmon et al. 1977; Simmons and Hoskins 1978; Lau 1979; Edmon et al. 1980; Chang et al. 2002). Baroclinic waves are associated with poleward eddy fluxes of heat, and thus vertically propagating wave activity, as they develop in the extratropical troposphere. When the waves reach the upper troposphere they dissipate, leading to equatorward fluxes of potential vorticity (e.g., Simmons and Hoskins 1978). If there is also meridional propagation of wave activity aloft, then the decay of baroclinic waves is associated with meridional eddy fluxes of momentum and thus accelerations in the barotropic component of the flow (e.g., Held 1975; Thorncroft et al. 1993).

Baroclinic waves do not exist in isolation. Rather they can form into coherent wave packets that propagate eastward via a mechanism called downstream development (Simmons and Hoskins 1979; Chang 1993; Lee and Held 1993). In this case, individual baroclinic eddies transfer their energy to downstream eddies, thus forming wave packets that propagate to the east at the group velocity of Rossby waves (e.g., Simmons and Hoskins 1979; Chang 1993; Chang et al. 2002). Under the right conditions, wave packets can propagate along an entire latitude circle, especially if they occur within the vicinity of a zonally coherent jet stream or waveguide (Hoskins and Ambrizzi 1993; Lee and Held 1993; Ambrizzi et al. 1995; Chang and Yu 1999; Chang 1999, 2005). Downstream development is important as it can bring storms (eddies) to regions where baroclinicity is weak. It is also responsible for the propagation of baroclinic activity from the North Pacific to the North Atlantic sector, where it can enhance storm development in the Atlantic storm track, a process often referred to as downstream seeding (e.g., Chang 1993).

Downstream development is widely accepted and understood. Recent research suggests that it is also accompanied by a hitherto overlooked aspect of extratropical wave packets: the coherent suppression of eddy activity following periods of enhanced baroclinic wave growth (Thompson et al. 2017, hereafter TCB17). In the Southern Hemisphere (SH), the suppression arises as eastward propagating wave packets consume mean potential energy and thus leave in their wake regions of anomalously low baroclinicity and wave growth. In contrast to the wave packet—which propagates to the east at roughly the group velocity of Rossby waves in upper troposphere, ~25–30 m s^{-1} (Lee and Held 1993; Chang 1993; Chang et al. 2002)—the suppression of baroclinicity propagates to the east at roughly the speed of the lower to midtropospheric flow (TCB17). Hence, the suppression of wave activity propagates to the east at a slower rate than the wave packet itself and appears in the wake (i.e., to the west) of the propagating wave packet.

A key aspect of the downstream suppression of wave activity in the Southern Hemisphere is that it gives rise to periodic behavior in various measures of extratropical storminess, including the eddy fluxes of heat, eddy kinetic energy (EKE), and precipitation (Thompson and Woodworth 2014; Thompson and Barnes 2014; Wang and Nakamura 2015, 2016; Wang et al. 2018). The periodicity peaks at ~20–30 days and is most clearly apparent when the SH circulation is averaged over a sufficiently

---

Corresponding author: Lina Boljka, lina.boljka@colostate.edu

DOI: 10.1175/JCLI-D-20-0483.1

broad longitudinal area to capture both the downstream development and attendant suppression of eddy activity (TCB17). Such periodicity is readily apparent in the SH, presumably because the storm track is sufficiently long there to allow downstream suppression to occur (TCB17). It is readily apparent in both dry dynamical core and full general circulation models (Thompson and Barnes 2014; Wang and Nakamura 2016; Boljka et al. 2018). It is readily apparent (albeit not explicitly noted) in simulations of downstream development in two-layer models (Lee and Held 1993; see Fig. 6c therein). And it is relatively weak but nevertheless significant in the Northern Hemisphere (NH) averaged over all longitudes (Thompson and Li 2015). Similar periodicity is theorized to arise in the North Atlantic storm track based on idealized numerical models (Ambaum and Novak 2014; Novak et al. 2015), but the evidence for subseasonal periodicity in the observed North Atlantic storm track remains unclear.

Downstream suppression has implications for our understanding of subseasonal variability in the extratropics, the behavior of simulated and observed extratropical wave packets, and the potential for subseasonal periodicity in extratropical weather. The goal of this study is to document the observational evidence for downstream suppression in both hemispheres. Previous work (TCB17) has shown that suppression plays an important role in driving subseasonal periodicity in the SH. But to date it is unclear whether such behavior is apparent in association with the NH storm tracks. The paper is structured as follows. Section 2 describes the data and methods. Section 3 reviews the evidence for downstream suppression in the SH, provides novel analyses of its spatial structure, and explores the evidence for such behavior in the NH. Section 4 provides an interpretation of the underlying mechanisms, and section 5 provides a summary and key conclusions.

2. Data and methods

The data used in this study are from the ERA-Interim observational reanalysis, which is provided by the European Centre for Medium-Range Weather Forecasts (Dee et al. 2011). The analyses are based on daily mean data for all calendar months over the time period 1 January 1979–31 December 2015. Data are analyzed on a 1.5° horizontal grid.

The eddy heat fluxes at 700 hPa and EKE at 300 hPa associated with baroclinic disturbances are found as follows (see also Thompson and Li 2015). The zonal (u) and meridional (v) wind as well as temperature (T) fields are analyzed on 6-hourly time scales. These 6-hourly fields are spatially filtered using harmonic analysis to retain variations associated with zonal wavenumbers (k) larger than 3 (i.e., $k > 3$). The filtering is done to emphasize fluctuations due to baroclinic waves (which have a typical zonal scale corresponding to zonal wavenumbers $k \approx 4$–8) relative to planetary-scale disturbances (which have a typical scale corresponding to zonal wavenumbers $k \approx 1, 2$). The filtering has almost no effect on results in the SH (as noted below), but it helps emphasize the variance due to baroclinic waves in the NH where the planetary waves have more substantial amplitude. Daily mean eddy quantities are then found by multiplying the respective 6-hourly filtered fields and averaging over successive 24-h periods. EKE is computed as $0.5(u'^2 + v'^2)$, whereas the eddy heat fluxes are computed as $v'T'$, where primes denote $k > 3$ filtered fields.

The seasonal cycle is removed from the daily mean temperature and eddy fields by subtracting the first four harmonics of the daily mean, climatological-mean annual cycle from each grid point. The lower tropospheric baroclinicity (b) is estimated as the anomalous meridional temperature gradient at 700 hPa, where the sign is defined such that positive values of b denote an enhanced equator-to-pole temperature gradient (i.e., $b = -\partial T/\partial y$ in the NH and $b = +\partial T/\partial y$ in the SH). Note that in principle, the baroclinicity is the meridional slope of the isentropes and thus includes the vertical temperature gradient, but that in practice is dominated by the meridional temperature gradient in the lower troposphere.

Details of the regression and composite analyses are described in the following sections where necessary. The statistical significance of the regression coefficients shown in Figs. 3 and 4 below is based on a two-tailed test of the t statistic at the 95% confidence level (i.e., a p value ≤ 0.05). The effective degrees of freedom are estimated as

$$D_t = n\frac{1 - r_1 r_2}{1 + r_1 r_2}, \tag{1}$$

where n is the number of days in the EKE time series, r_1 and r_2 are the lag-one day autocorrelations of the two time series used in the regression, and D_t is the effective degrees of freedom (Bretherton et al. 1999). In all analyses conducted here $D_t > 7000$. Note that for Figs. 3 and 4 below we first determine the minimum correlation coefficient that exceeds the 95% significance threshold, and then convert the minimum correlation coefficient (r) to a minimum regression coefficient by multiplying the minimum r by the standard deviation of the (regressed) EKE time series.

The power spectra are computed as follows. First we split the data into equal length and overlapping subsets of the full time series. We choose 1024 day-long subsets with a 512-day overlap. This gives 25 overlapping subsets and a lowest resolvable frequency of 1/1024 day^{-1}. The subsets are smoothed using a Hanning window and then converted to the frequency domain using Fourier transform. The resulting power spectra are then averaged over all 25 subsets to obtain the gray lines shown below in Fig. 2. The spectra are smoothed to further increase the number of degrees of freedom of each independent spectral estimate by applying a 10-point running mean in the frequency domain (black line in Fig. 2).

The number of degrees of freedom for each independent spectral estimate is approximately 260, determined as $f_\omega n/M$, where n is again the number of days in the EKE time series, $M = 512$ is the number of independent spectral estimates in the unsmoothed power spectra, and $f_\omega = 10$ accounts for the smoothing of spectral estimates in the frequency domain. The shapes of the red-noise fits are found from the lag-one autocorrelation of the 20-day high-pass filtered (using a Lanczos filter; Duchon 1979) time series as per Gilman et al. (1963) and Thompson and Li (2015). The fits are scaled such that the variances of the fits are identical to the variances of the respective EKE time series (i.e., the area under the EKE spectra and the red-noise fits are identical). The 95% confidence curves are found by multiplying the red-noise fits by the

χ^2 statistic for a two-sided p value of 0.05 (see also Madden and Julian 1971).

3. Downstream suppression of wave packets

In this section we document the observational support for downstream suppression of wave packets in both hemispheres. Select results for the SH are reproduced from TCB17 for two reasons: (i) they provide context for the amplitude of downstream suppression in the NH; and (ii) the results in TCB17 are based on unfiltered data and are thus reproduced here for disturbances of zonal wavenumber $k > 3$. We begin by exploring Hovmöller plots of upper tropospheric EKE in the Southern and Northern Hemispheres.

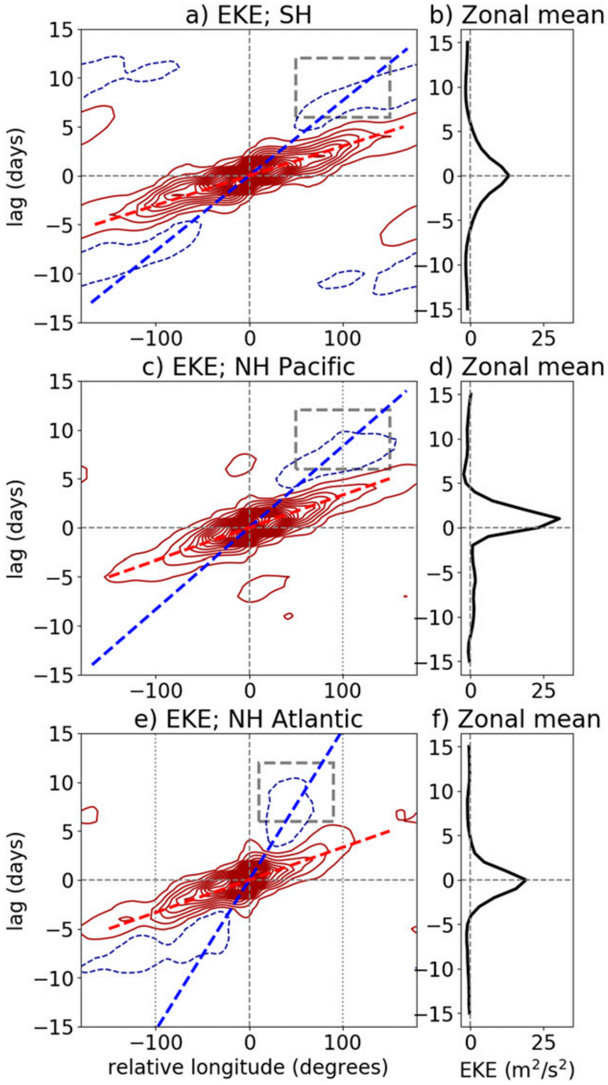

FIG. 1. (left) Hovmöller plot of EKE at 300 hPa averaged meridionally (a) between 35° and 60°S and (c),(e) between 35° and 60°N. Results show daily and meridional-mean EKE regressed as a function of lag and longitude onto standardized values of EKE at base longitude λ. The abscissa indicates the relative longitude of the regression. Results are averaged over λ that span all SH longitudes in (a), longitudes in the North Pacific sector (between 150° and 210°E) in (c), and longitudes in the North Atlantic sector (between 300° and 360°E) in (e). (right) Zonal averages of the results from the left column averaged over (b) all longitudes, (d) the longitudes spanned by the vertical gray dashed and dotted lines in (c), and (f) the longitudes spanned by the vertical gray dotted lines in (e). The contour interval is 4 $\mathrm{m^2\,s^{-2}}$ (i.e., . . . , −6, −2, 2, 6, . . .) with blue denoting negative contours and red denoting positive contours. The lowest contour value ($\pm 2\,\mathrm{m^2\,s^{-2}}$) corresponds closely to the 95% significance threshold. Blue and red dashed lines represent typical speeds of the lower-tropospheric and upper-tropospheric flows, respectively, estimated based on the regression analysis in this figure: ~11 and ~27.5 $\mathrm{m\,s^{-1}}$ in (a), ~10 and ~25 $\mathrm{m\,s^{-1}}$ in (c), and ~5.5 and ~25 $\mathrm{m\,s^{-1}}$ in (e) (as measured at 45° latitude). Results are smoothed with a 20° running mean in longitude for display purposes only. The gray dashed boxes are the bounds used in Fig. 3. See text for further details.

a. Southern Hemisphere

Figure 1a shows the Hovmöller plot for EKE at 300 hPa averaged meridionally over the SH midlatitudes between 35° and 60°S (hereafter EKE$_{35\text{–}60\mathrm{S}}$). The Hovmöller plot is formed as follows. First we form a standardized base time series of EKE$_{35\text{–}60\mathrm{S}}$ at longitude λ. Then we regress EKE$_{35\text{–}60\mathrm{S}}$ at all longitudes and all lags from −15 to +15 days onto the standardized base time series to form a Hovmöller plot for EKE$_{35\text{–}60\mathrm{S}}$ centered on longitude λ. This step is repeated for standardized base time series at all longitudes $0° \leq \lambda < 360°$E. Finally, the individual Hovmöller plots calculated for each base time series (at base longitude λ) are averaged to form a composite Hovmöller plot of EKE$_{35\text{–}60\mathrm{S}}$ for the Southern Hemisphere. The results are then plotted as a function of relative longitude (relative to the base longitude) and lag (Fig. 1a). The results are smoothed with a 20° running mean in longitude for display purposes only.

The resulting composite Hovmöller plot is consistent with that shown in TCB17 (their Fig. 3) for unfiltered data. By construction, the largest positive EKE anomalies are found at lag 0 and relative longitude 0. Downstream *development* is apparent as the pattern of positive EKE anomalies that propagate to the east at speeds comparable to the Rossby group velocity in the upper troposphere (the red dashed line indicates speeds of 27.5 $\mathrm{m\,s^{-1}}$). Downstream *suppression* is apparent as the relatively weak negative EKE contours that form to the west of the main wave packet as it propagates eastward with time. The negative anomalies form ~100° to the east of the base longitude ~6–12 days following the peak in EKE. That is, they form along an isotach corresponding closely to the speed of the lower-midtropospheric flow (the blue dashed line indicates speeds of 11 $\mathrm{m\,s^{-1}}$). Note that once the suppression in the EKE in the upper troposphere occurs, the negative anomalies in EKE propagate to the east at roughly the same rate as the original wave packet (i.e., at roughly the Rossby group velocity in the upper troposphere).

The negative EKE anomalies associated with downstream suppression are much weaker than the positive EKE anomalies associated with downstream development. However, the negative anomalies are not only statistically significant (as shown below), they are also critically important in driving the time dependent behavior of EKE when averaged zonally over the midlatitudes. This is because the negative anomalies form as the positive

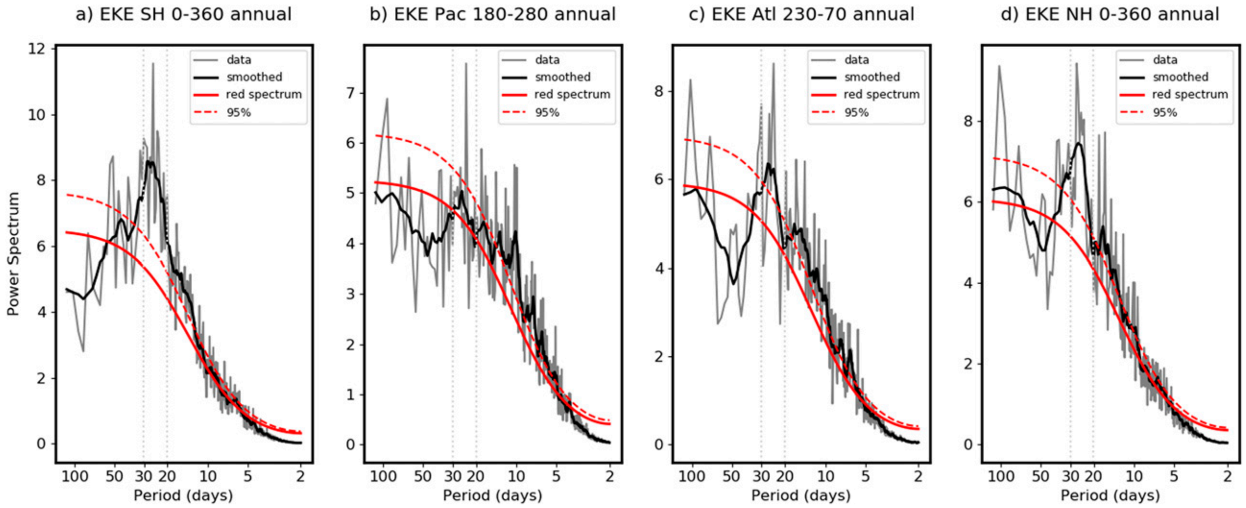

FIG. 2. Power spectra of EKE time series averaged meridionally (35°–60° latitude) and longitudinally in (a) the SH (zonal mean), (b) the NH Pacific (averaged between 180° and 280°E), (c) the NH Atlantic (averaged between 230° and 70°E), and (d) the NH (zonal mean). The gray solid lines denote unsmoothed spectra averaged over 25 overlapping subsets of the data; the black solid lines show the spectra after applying a 10-point running mean to the gray spectral estimates; the red solid lines indicate the red-noise fit; and the red dashed lines correspond to the 95% significance levels. See text for more details.

anomalies decay and are thus not fully opposed by the positive anomalies when the circulation is averaged over broad zonal bands. As a result, there are negative side lobes in the zonally averaged EKE regressions at lags longer than about ±7 days (Fig. 1b) and pronounced periodicity in the power spectrum for SH EKE averaged over all longitudes (Fig. 2a; see also Thompson and Woodworth 2014; Thompson and Barnes 2014, TCB17).

b. Northern Hemisphere

Is a similar pattern of downstream suppression apparent in association with wave packets in the Northern Hemisphere? The NH storm tracks are less zonally coherent than their SH counterpart. Wave packets in the SH are capable of propagating around the entire latitudinal circle (i.e., the positive EKE anomalies in Fig. 1a span all longitudes; see also Lee and Held 1993), whereas wave packets in the NH become less coherent as they move over continental regions (Chang et al. 2002). For this reason, analyses of NH extratropical cyclones are frequently explored separately over the North Pacific and the North Atlantic storm track regions.

Figures 1c and 1e are constructed in the same manner as Fig. 1a, but here the EKE time series are averaged over the NH midlatitudes between 35° and 60°N (hereafter $\mathrm{EKE}_{35\text{–}60\mathrm{N}}$). The Hovmöller plots are averaged over base longitudes centered on two zonal sectors: the North Pacific storm track region (150°–210°E; Fig. 1c) and the North Atlantic storm track region (300°–360°E; Fig. 1e). Note that (i) the SH composite Hovmöller plot is symmetric in time and space since the results are averaged over all longitudes, but that (ii) there is no such constraint on the NH composite Hovmöller plots since they are averaged over select regions of the hemisphere.

As expected, both sectors indicate downstream development in which positive EKE anomalies propagate to the east at speeds characteristic of the group velocity in the upper troposphere (the red dashed lines in Figs. 1c and 1e indicate speeds of $25\,\mathrm{m\,s^{-1}}$). The positive EKE anomalies extend farther eastward from the base region (150°–210°E) in regressions for the North Pacific and farther westward from the base region (300°–360°E) in regressions for the North Atlantic. The differences in downstream development over the two sectors are consistent with the facts that (i) eddy activity in the North Pacific storm track frequently “seeds” the North Atlantic (the regressions at relative longitude 100° downstream from the base longitude in Fig. 1c lie in the North American sector), and (ii) eddy activity in the North Atlantic storm track does not readily extend across Eurasia (Fig. 1e; see also Chang et al. 2002). Overall, downstream development in both NH storm tracks is more zonally confined than it is in the SH.

Importantly, regressions centered on both NH sectors also reveal centers of action that are consistent with downstream suppression. Negative regression values are evident downstream of the North Pacific storm track (Fig. 1c), and both upstream and downstream of the North Atlantic storm track (Fig. 1e). The negative center of action downstream of the North Pacific emerges about 100° to the east of the peak positive anomaly and is found along the $\sim 10\,\mathrm{m\,s^{-1}}$ trajectory (blue dashed line). The negative center of action downstream of the North Atlantic storm track emerges ~30° to the east of the peak positive anomaly and is found along the $\sim 5\,\mathrm{m\,s^{-1}}$ trajectory (blue dashed line). As is the case in the SH, the negative anomalies in the North Pacific sector propagate eastward at the speed of the upper-tropospheric group velocity. The negative anomalies upstream of the North Atlantic storm track also propagate eastward at the speed of the upper-tropospheric group velocity, but it is more difficult to assess the propagation speed of the negative anomalies downstream of the storm track.

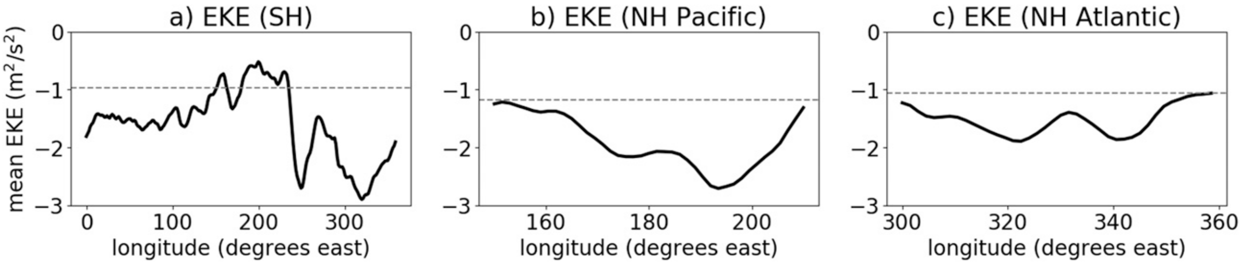

FIG. 3. Lag regression coefficients averaged over the gray dashed boxes in Figs. 1a, 1c, and 1e for base longitudes indicated. (a) Results averaged over time lags from +6 to +12 days and spatial lags from +50° to +150° longitude and shown for all base longitudes in the SH. (b) As in (a), but for time lags from +6 to +12 days and spatial lags from +50° to +150° longitude for base longitudes in the North Pacific sector. (c) As in (b), but for time lags from +6 to +12 days and spatial lags from +10° to +90° longitude for base longitudes in the North Atlantic sector. The horizontal gray dashed line corresponds to the 95% significance level as discussed in the text.

The differences in the locations of downstream suppression in the North Pacific and North Atlantic sectors are consistent with the differences in the speed of the lower to midtropospheric flow over regions downstream of both sectors. That is: the tropospheric flow is generally weaker over regions downstream of the North Atlantic storm track than it is over regions downstream of the North Pacific storm track. It is less clear why there is no robust negative EKE anomaly at negative lags over the North Pacific sector. However, the absence of negative anomalies at negative lags may simply reflect the zonal boundary of the storm track and its influence on the zonal asymmetry of wave packets (e.g., Swanson and Pierrehumbert 1994). Note that analogous asymmetry between negative and positive lags was not found in analyses of comparably sized zonal bands in the SH (not shown).

The zonal averages of the NH Hovmöller plots are shown in Figs. 1d and 1f. Here the zonal averages are computed over the longitudinal bands where downstream development and suppression is apparent in Figs. 1c and 1e, as indicated by the vertical gray lines on the figures. That is, the zonal averages are computed (i) between the base longitude (0° relative longitude) and 100° downstream of it in the North Pacific sector (note the vertical gray dashed and dotted lines in Fig. 1c), and (ii) between 100° upstream and 100° downstream of the base longitude in the North Atlantic sector (note the vertical gray dotted lines in Fig. 1e). As such, the North Pacific results are representative of EKE variability in the 180°–280°E longitudinal band, and the North Atlantic results are representative of EKE variability in the 230°–70°E longitudinal band. As is the case in the SH, the negative EKE anomalies that characterize downstream suppression lead to weak—but important—negative side lobes in the zonal mean of the $\mathrm{EKE}_{35\text{–}60\mathrm{N}}$ regressions.

The negative side lobes in the NH zonal mean EKE regressions are weaker than their SH counterparts. Nevertheless, they are associated with periodicity in $\mathrm{EKE}_{35\text{–}60\mathrm{N}}$ over the NH storm track regions. The periodicity is relatively weak over the North Pacific storm track (Fig. 2b) but it is more pronounced and statistically significant over the North Atlantic storm track (Fig. 2c). Consistent with Thompson and Li (2015) the periodicity clearly extends to the zonal mean (Fig. 2d). The observed periodicity in the North Atlantic storm track is consistent with the observed downstream suppression there (Fig. 1e) and also provides a measure of observational support for the baroclinic oscillator model of Ambaum and Novak (2014). The periodicity in the NH zonal mean is weaker than that in the SH zonal mean (cf. Figs. 2a,d), but is both robust and statistically significant.

The results shown in Figs. 1a, 1c, and 1e are composites found by averaging Hovmöller plots formed for base longitudes within the three broad zonal bands: 0°–360°E for the SH, 150°–210°E for the North Pacific, and 300°–360°E for the North Atlantic. Figure 3 explores the amplitude and significance of downstream suppression within each of those zonal sectors. The amplitude of downstream suppression for any given base longitude is defined as the regression coefficients averaged over the gray dashed boxes in the appropriate panel from Fig. 1. The 95% significance thresholds are found as discussed in section 2 and indicated by the horizontal dashed lines. The largest downstream suppression in the SH occurs for wave packets that originate around 250°–350°E (Fig. 3a), the largest suppression associated with the North Pacific sector occurs for wave packets that originate around 180°–200°E (Fig. 3b), and the largest suppression associated with the North Atlantic sector occurs for wave packets that originate around 320°–340°E (Fig. 3c). Downstream suppression is statistically significant for wave packets originating in all of these regions (i.e., the regressions far exceed the 95% significance threshold).

c. *Spatial evolution*

Figure 4 provides a synoptic perspective of downstream suppression originating in the vicinity of the key base longitudes identified in Fig. 3, and listed in Table 1. Again, we start with results for the SH. The top row of Fig. 4 shows EKE as a function of latitude, longitude, and lag regressed onto EKE averaged over the box spanning 35°–60°S and 240°–260°E, which lies to the west of southern South America. Results are shown at intervals of 3-day lags, starting from a lag of −3 days (left column) to a lag of +12 days (right column). Stippling indicates results that are significant at the 95% level as discussed in section 2. By construction, the largest EKE anomalies are found at lag 0 within the region of analysis. The region of positive EKE anomalies proceeds eastward (clockwise as indicated by the arrow) across the Southern Ocean between lags −3 and +3 days in accordance with downstream development. The downstream suppression of the EKE anomalies is

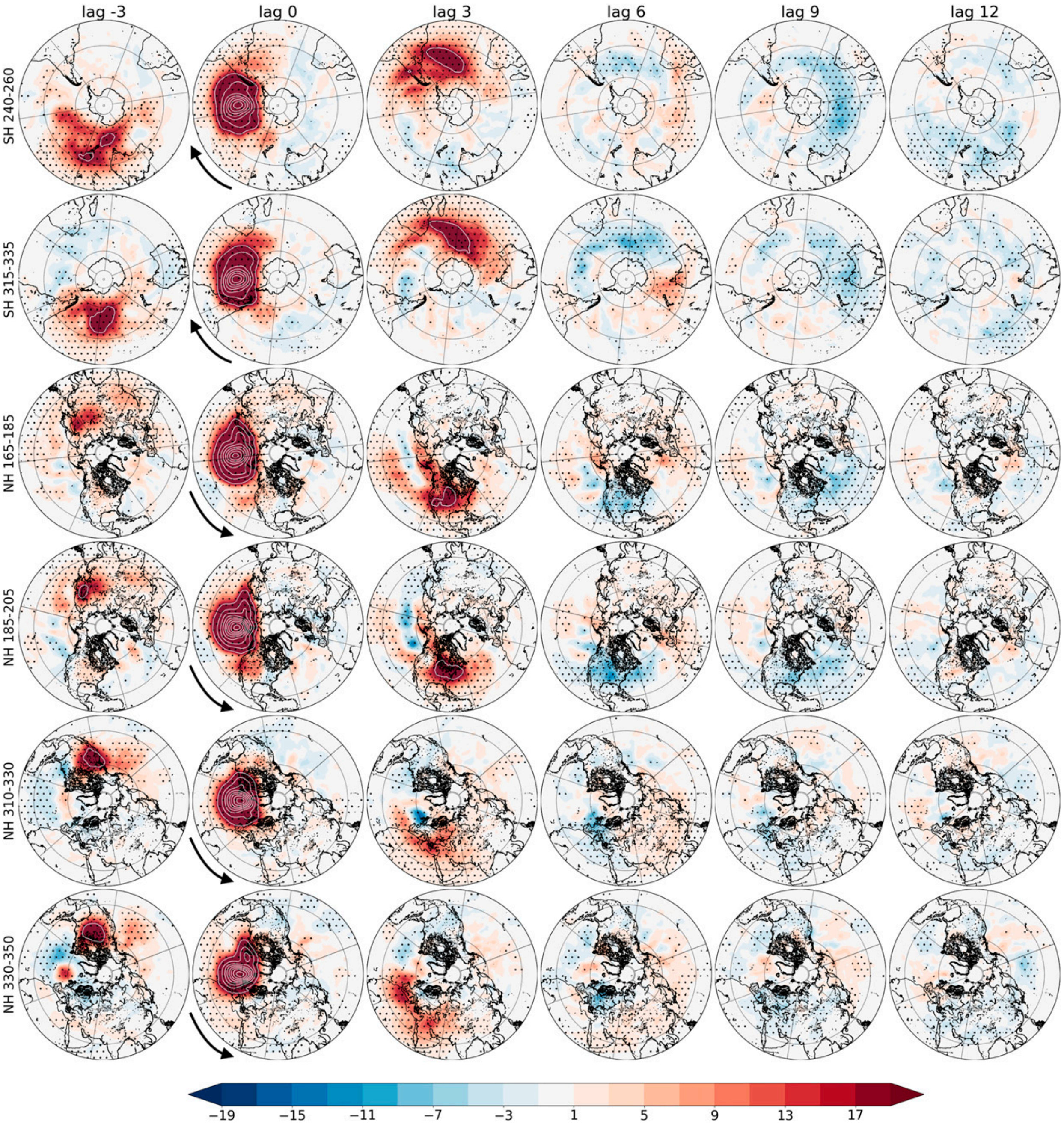

FIG. 4. Latitude–longitude lag regression of daily mean synoptic-scale EKE at lags −3, 0, 3, 6, 9, and 12 onto standardized time series of EKE averaged between 35° and 60° latitude and over 20° longitude bands as labeled (see also Table 1): (first row) 240°–260°E, (second row) 315°–335°E, (third row) 165°–185°E, (fourth row) 185°–205°E, (fifth row) 310°–330°E, and (sixth row) 330°–350°E. The top two rows are computed for SH EKE, and thus eastward is clockwise (as indicated by the arrows in the bottom left corner of lag 0). The bottom four rows are computed for NH EKE, and thus eastward is anticlockwise (as indicated by the arrows in the bottom left corner of lag 0). All panels were rotated so that the longitudes used as a basis for the regression are located at 9 o'clock. The contour interval is 20 $m^2 s^{-2}$, and the 0th contour is omitted for clarity (i.e., . . . , −40, −20, 20, 40, . . .). Stippling denotes values that are statistically significant at the 95% level.

apparent as the region of negative EKE anomalies that begin to form around lag +6 days and span much of the southern Indian Ocean by lag +9 days.

The second row in Fig. 4 shows analogous results for another representative region in the SH, in this case the box spanning 35°–60°S and 315°–335°E, which lies in the South Atlantic Ocean. Note that the maps are rotated relative to the top row so that the base region of the analysis again lies at 9 o'clock in all panels. As is the case in the top row, the region of positive EKE anomalies exhibits downstream development for lags

TABLE 1. Latitude–longitude boxes, over which EKE daily time series is averaged, before regressions onto it are performed in Fig. 4.

Region	Latitude range	Longitude range
SH 240–260	35°–60°S	120°–100°W
SH 315–335	35°–60°S	45°–25°W
NH Pacific 165–185	35°–60°N	165°E–175°W
NH Pacific 185–205	35°–60°N	175°–155°W
NH Atlantic 310–330	35°–60°N	50°–30°W
NH Atlantic 330–350	35°–60°N	30°–10°W

from −3 to +3 days. Downstream suppression is apparent as a region of negative EKE anomalies that peak around lag +9 days, this time to the south of Australia.

The remaining rows in Fig. 4 show the companion results for longitudes centered in the North Pacific (rows 3 and 4) and the North Atlantic (rows 5 and 6) sectors. The maps are again rotated so that the base region of the analysis lies at 9 o'clock in all panels. Note that eastward (indicated by the arrows) now lies in the counterclockwise direction. EKE anomalies originating in the North Pacific sector (rows 3 and 4) exhibit downstream development over the North American continent by lag +3 days that also act to seed the North Atlantic storm track (Chang et al. 2002; Thompson and Li 2015). The sign of the anomalies reverses by lag 6 days, and by lag 9 days the North Atlantic sector is spanned by negative EKE anomalies. In other words: downstream *development* from the North Pacific acts to seed storminess in the North Atlantic storm track on time scales of a few days, while the subsequent downstream *suppression* acts to weaken it on time scales of about a week.

Results for EKE anomalies originating in the North Atlantic sector (rows 5 and 6 in Fig. 4) also exhibit downstream development and suppression; however, here the EKE evolution is relatively slow and more zonally confined (as also noted above and shown in Fig. 1e). The largest positive EKE anomalies extend across the Mediterranean at a lag of +3 days. The most pronounced negative anomalies span western Europe (row 5) and eastern Europe (row 6) at a lag of 6 days and much of Eurasia at lags of 9–12 days. The downstream suppression of EKE anomalies originating in the North Atlantic storm track is statistically significant (Fig. 3c) but is generally much weaker than it is for anomalies that originate in the SH and the North Pacific storm tracks (see also Fig. 3).

4. Interpretation

The observed periodicity in the Southern Hemisphere (Fig. 2a) is consistent with two-way feedbacks between tropospheric baroclinicity and baroclinic wave growth (Thompson and Barnes 2014; see also Stone 1978; Thompson and Birner 2012). The proposed mechanism works in a manner consistent with the baroclinic adjustment (Stone 1978): (i) periods of anomalously high baroclinicity lead to positive tendencies in baroclinic wave growth and thus the poleward fluxes of heat; (ii) anomalously poleward fluxes of heat, in turn, lead to negative tendencies in the baroclinicity; and (iii) negative tendencies in the baroclinicity lead to anomalously low baroclinicity and thus negative tendencies in the poleward fluxes of heat. The resulting oscillation is damped by diabatic processes such as friction and radiative cooling. A similar mechanism also lies at the root of idealized models of the North Atlantic storm track (Ambaum and Novak 2014; Novak et al. 2015). However, other studies have very different interpretations. For example, Wang and Nakamura (2016) argue that periodicity such as that shown in Fig. 2a can arise from wave–wave interactions between disturbances of different frequencies, and Zurita-Gotor (2017) argues that periodicity in the heat fluxes can arise from out-of-phase relationships between the fluxes associated with planetary and synoptic-scale eddies.

TCB17 extended the "baroclinic oscillator" model from Thompson and Barnes (2014) to include (i) two-way coupling between the heat fluxes and baroclinicity in the lower troposphere and (ii) generation of wave activity in the upper troposphere by the lower tropospheric heat fluxes. In their model, the coupling between the heat fluxes and the baroclinicity is advected eastward at flow speeds characteristic of the lower-midtropospheric flow (U_{low}) whereas the signature of the oscillation in upper tropospheric wave activity is advected eastward at a rate consistent with the upper tropospheric group velocity (U_{up}). As noted in TCB17, assigning propagation speeds such that $U_{\mathrm{up}} > U_{\mathrm{low}}$ ensures that successive phases of the oscillation in the heat flux ($v'T'$) in the lower troposphere will emerge as an east–west dipole in EKE anomalies in the upper troposphere, such that successive phases of the oscillation in EKE (i.e., downstream suppression) emerge to the west of–rather than at the same longitude as the previous phase.

Here we propose a simplification of the model from TCB17 that is likewise capable of simulating the broad characteristics of downstream suppression. As in Thompson and Barnes (2014), the model is based on two equations that simulate wave-mean flow interactions in the extratropical troposphere: (i) a prognostic equation for the extratropical baroclinicity b that derives from the first law of thermodynamics, and (ii) a prognostic equation for extratropical eddy heat flux $v'T'$ that is motivated by baroclinic instability theory and the diffusive nature of the heat fluxes (e.g., Lindzen and Farrell 1980; Hoskins and Valdes 1990). As in TCB17, the model includes zonal advection of the baroclinicity and the heat fluxes. However, unlike TCB17 we allow for different advection speeds of the two quantities, and we do not include an equation for the relationship between the heat fluxes and eddy kinetic energy. The assumption that the baroclinicity and heat fluxes can be advected at different rates follows from the premises that (i) the heat fluxes reflect the wave packet and thus propagate at a speed consistent with the Rossby group velocity and (ii) the baroclinicity is influenced by the (relatively fast) wave packet but is also advected by the (relatively slow) mean flow. That the heat fluxes reflect the wave packet is supported by fact that they are intrinsically linked to variations in extratropical wave trains and their wave activity (e.g., Chang 1993, cf. Fig. 8). This means that in the budgets below the EKE is implicitly present as it can have two-way feedbacks with both the heat flux (EKE and/or wave activity budget) and the baroclinicity (non-acceleration theorem) (e.g., Vallis 2006).

The model can be expressed as follows:

$$\frac{\partial b}{\partial t} + U_b \frac{\partial b}{\partial x} = \alpha_b v'T' - \frac{b}{\tau_b}, \tag{2}$$

$$\frac{\partial v'T'}{\partial t} + U_{vT} \frac{\partial v'T'}{\partial x} = \alpha_{vT} b - \frac{v'T'}{\tau_{vT}}, \tag{3}$$

TABLE 2. Parameters used in the theoretical model, Eqs. (2) and (3). See also TCB17.

Parameter	Value
α_b	$3.7 \times 10^{-13}\,\mathrm{m}^{-2}$
α_{vT}	$-23.6\,\mathrm{m}^2\,\mathrm{s}^{-2}$
τ_b	4 days
τ_{vT}	2 days

where b and $v'T'$ denote the baroclinicity and eddy fluxes of heat, respectively; α_b indicates the amplitude of the forcing of the baroclinicity by the heat fluxes; α_{vT} indicates the amplitude of the forcing of the heat fluxes by the baroclinicity; τ_b and τ_{vT} are linear damping coefficients; U_b represents the advection speed of the baroclinicity; and U_{vT} represents the advection speed of wave activity (as well as Rossby group velocity).

The feedback parameters α_b and α_{vT} are found from observations as in TCB17 by (i) forming time series of the observed heat fluxes and baroclinicity averaged zonally and meridionally over the midlatitude region (35°–60° latitude), and (ii) regressing the observed tendencies in the midlatitude-mean baroclinicity onto the midlatitude-mean heat fluxes, and vice versa. The damping coefficients τ_b and τ_{vT} are found from the autocorrelation functions of the respective midlatitude-mean baroclinicity and heat flux time series. The parameters used here are identical to those used in TCB17 and are listed in Table 2. Note that the sign of the coefficients is such that (i) an increase in the equator-to-pole temperature gradient leads to a positive tendency in the poleward heat fluxes, consistent with the diffusive nature of the heat fluxes and (ii) an increase in the poleward heat fluxes leads to a negative tendency in the equator-to-pole temperature gradient, consistent with the effects of temperature advection by the eddies.

The zonal-mean structure of the output is independent of the advective terms and is characterized by periodicity in the heat fluxes on a time scale of ~20–25 days (not shown; Thompson and Barnes 2014; TCB17). However, the west–east structure of the output is determined by the advection rates U_b and U_{vT} and varies greatly depending on their relative amplitudes. In the case where $U_b = U_{vT} = 0$, the oscillation is fixed in space. In the case where $U_b = U_{vT} > 0$, then the oscillation is fixed in a coordinate system that moves with the flow. And as shown in Fig. 5, if $U_{vT} > U_b$ then the oscillation lags the wave packet as it moves toward the east.

The two panels in Fig. 5 show the simulated heat fluxes (Fig. 5a) and baroclinicity (Fig. 5b) as a function of longitude and time for advection rates of $U_{vT} = 25\,\mathrm{m\,s}^{-1}$ and $U_b = 10\,\mathrm{m\,s}^{-1}$. The advection rates are chosen since they are comparable to typical Rossby group velocity (in the upper troposphere) and the speed of the lower to midtropospheric flow, respectively. Note that the baroclinicity is thus advected by the mean flow at a rate of $10\,\mathrm{m\,s}^{-1}$ but still "sees" the faster propagating wave packet via the term $\alpha_b v'T'$, and that the wave packet is advected at the Rossby group velocity but still "sees" the slower moving baroclinicity via the term $\alpha_{vT} b$. The model is initiated with a positive heat flux anomaly that has an amplitude corresponding to the standard deviation of the eddy heat fluxes (~$27.3\,\mathrm{m\,K\,s}^{-1}$) and a Gaussian shape with a width of 8° longitude.

As the integration begins, the primary wave packet moves eastward at a rate given by the Rossby group velocity U_{vT} (red

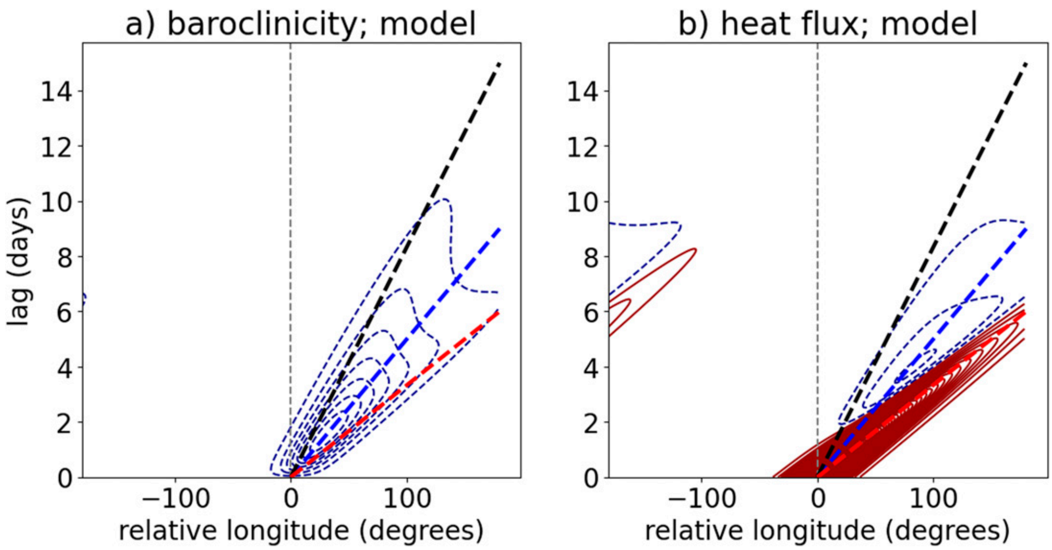

FIG. 5. The evolution of (a) baroclinicity and (b) heat flux via the theoretical model in Eqs. (2) and (3). For details of the model see text. Blue and red contours represent negative and positive values, respectively. The sign of the anomalies is such that the positive values denote increases in the equator-to-pole temperature gradient and the poleward fluxes of heat in both hemispheres. The black dashed line represents $10\,\mathrm{m\,s}^{-1}$, the blue dashed line represents $16.7\,\mathrm{m\,s}^{-1}$, and the red dashed line represents $25\,\mathrm{m\,s}^{-1}$. The contour interval for the baroclinicity is $0.8 \times 10^{-7}\,\mathrm{K\,m}^{-1}$ (i.e., . . . , −1.2, −0.4, 0.4, . . .). The contour interval for the heat fluxes is $0.4\,\mathrm{K\,m\,s}^{-1}$ (i.e., . . . , −0.6, −0.2, 0.2, . . .).

dashed line). This drives negative baroclinicity anomalies (i.e., a reduction in the equator-to-pole temperature gradient). Importantly, the baroclinicity anomalies do not simply track the wave packet as it moves to the east, but are spread to the west of the wave packet since the baroclinicity anomalies generated by the wave packet are advected eastward at a slower rate (U_b, black dashed line) than the wave packet itself. As such, the model gives rise to a broad region of negative baroclinicity anomalies that lies between the U_b and U_{vT} isotachs (black and red dashed lines), peaking at an isotach in between (here it is ~16.7 m s^{-1}; blue dashed line). The baroclinicity anomalies not only act to reduce the amplitude of the initial heat flux anomalies but—importantly—also give rise to a region of negative heat flux anomalies (i.e., a suppression) to the west of the wave packet, emerging along the isotach corresponding to peak baroclinicity (blue dashed line). In other words, the baroclinicity is influenced not only by the wave packet (via $\alpha_b v'T'$) but also by the mean flow (via $U_b \partial b/\partial x$), and thus leads to the development of negative heat flux anomalies that are broadly consistent with downstream suppression (discussed above).

Figure 6 shows the corresponding results for observations in the Southern Hemisphere, North Atlantic, and North Pacific storm tracks. The panels in Fig. 6 are constructed in a similar manner to Fig. 1. The left column shows b at 700 hPa regressed on the same basis EKE time series used to construct Figs. 1a, 1c, and 1e; the left column shows attendant results for the eddy fluxes of heat at 700 hPa. Again, the sign of the baroclinicity is such that positive values denote an enhanced equator-to-pole temperature gradient in both hemispheres, and the sign of the heat fluxes is such that positive values denote enhanced poleward heat fluxes. The red and blue dashed lines are reproduced from Fig. 1 and denote the path followed by the upper-tropospheric wave packet (red dashed lines) and downstream suppression (blue dashed lines).

Consider first the results for the Southern Hemisphere, as also highlighted in TCB17. The results are dominated by three primary features that to first order bear close resemblance to the output of the simple model: (i) the envelope of the eddy heat fluxes (Fig. 6d)—and thus of the wave packet—is stretched along the path of the Rossby group velocity and hence of downstream development (red dashed line); (ii) negative heat flux anomalies form around lags 3–10 days to the west of the primary wave packet (Fig. 6d), consistent with the pattern of downstream suppression evident in the EKE field (Fig. 1a); and (iii) the attendant baroclinicity anomalies are dominated by a period of low baroclinicity (blue contours in Fig. 6a) that closely follows the period of largest heat flux anomalies (red contours in Fig. 6d) and precedes the period of negative heat flux anomalies (blue contours in Fig. 6d).

Figures 6b, 6c, 6e, and 6f show analogous results for the North Pacific and North Atlantic sectors. To leading order, the North Pacific results (Figs. 6b,e) are similar to those found in the model and in the SH, albeit with additional positive baroclinicity anomalies at lags greater than ~5 days (Fig. 6b). Again, the largest $v'T'$ anomalies (red contours in Fig. 6e) are followed by negative baroclinicity anomalies around lags from +1 to +5 days (blue contours in Fig. 6b), and these negative baroclinicity anomalies are followed by relatively weak heat flux anomalies (blue contours in Fig. 6e) that emerge along the isotach of the peak baroclinicity anomalies (blue dashed line in Fig. 6e). Results for the North Atlantic also indicate robust negative baroclinicity anomalies for lags from +1 to +9 days (blue contours in Fig. 6c). The resulting anomalies in the heat fluxes (Fig. 6f) are less clear than those found in the SH and North Pacific sectors, but the sign of the results nevertheless supports the notion that downstream suppression arises from two-way interactions between eastward propagating wave packets and the underlying baroclinicity.

5. Concluding remarks

Individual synoptic eddies are marked by baroclinic conversions of mean potential energy to eddy kinetic energy as the disturbance grows, followed by barotropic conversions of eddy kinetic energy to zonal-mean kinetic energy as the disturbance decays (Simmons and Hoskins 1978). Such eddies frequently do not occur in isolation. Rather as they decay they can transfer energy to developing eddies downstream. The resulting *downstream development* of baroclinic waves gives rise to coherent packets of eddy activity that propagate eastward in the upper troposphere at roughly the Rossby group velocity there, ~25–30 m s^{-1} (e.g., Simmons and Hoskins 1979; Chang 1993).

This paper is concerned with another seemingly robust aspect of baroclinic waves: the *downstream suppression* of baroclinic wave activity, where “downstream” refers to regions downwind of the original disturbance. As baroclinic wave packets propagate eastward, they act to reduce the mean potential energy below its climatological mean value. As such, periods following the passage of a baroclinic wave packet are marked by lower than normal baroclinicity and thus suppressed eddy growth. The downstream suppression of baroclinic wave activity has much smaller amplitude than downstream development. However, it is important for two key reasons: (i) it is associated with suppressed wave activity on time scales at the limit of deterministic weather forecasting (Figs. 1 and 4) and (ii) it gives rise to statistically significant periodicity in various eddy statistics on subseasonal time scales (Fig. 2). In our previous work (TCB17), we identified the role of the suppression of wave activity in forming periodic behavior in the SH. Here we extended that work to explore and contrast downstream suppression in both hemispheres.

In the Southern Hemisphere, downstream suppression is marked by a reduction in eddy kinetic energy that emerges roughly 100° to the east and ~1 week after largest amplitude in the original wave packet (Figs. 1a and 4). In contrast to downstream development, which propagates to the east at ~25–30 m s^{-1}, the suppression of EKE anomalies propagates eastward at ~10 m s^{-1}, which is comparable to the speed of the lower to midtropospheric flow. Very similar suppression is found in the Northern Hemisphere storm tracks, albeit with varying amplitudes and time scales (Figs. 1c,e and 4). In the North Pacific (Fig. 1a), downstream suppression exhibits a very similar temporal/spatial structure to that found in the Southern Hemisphere (Fig. 1a). In the North Atlantic, it exhibits a very similar time scale to that found in the Southern Hemisphere, but is more

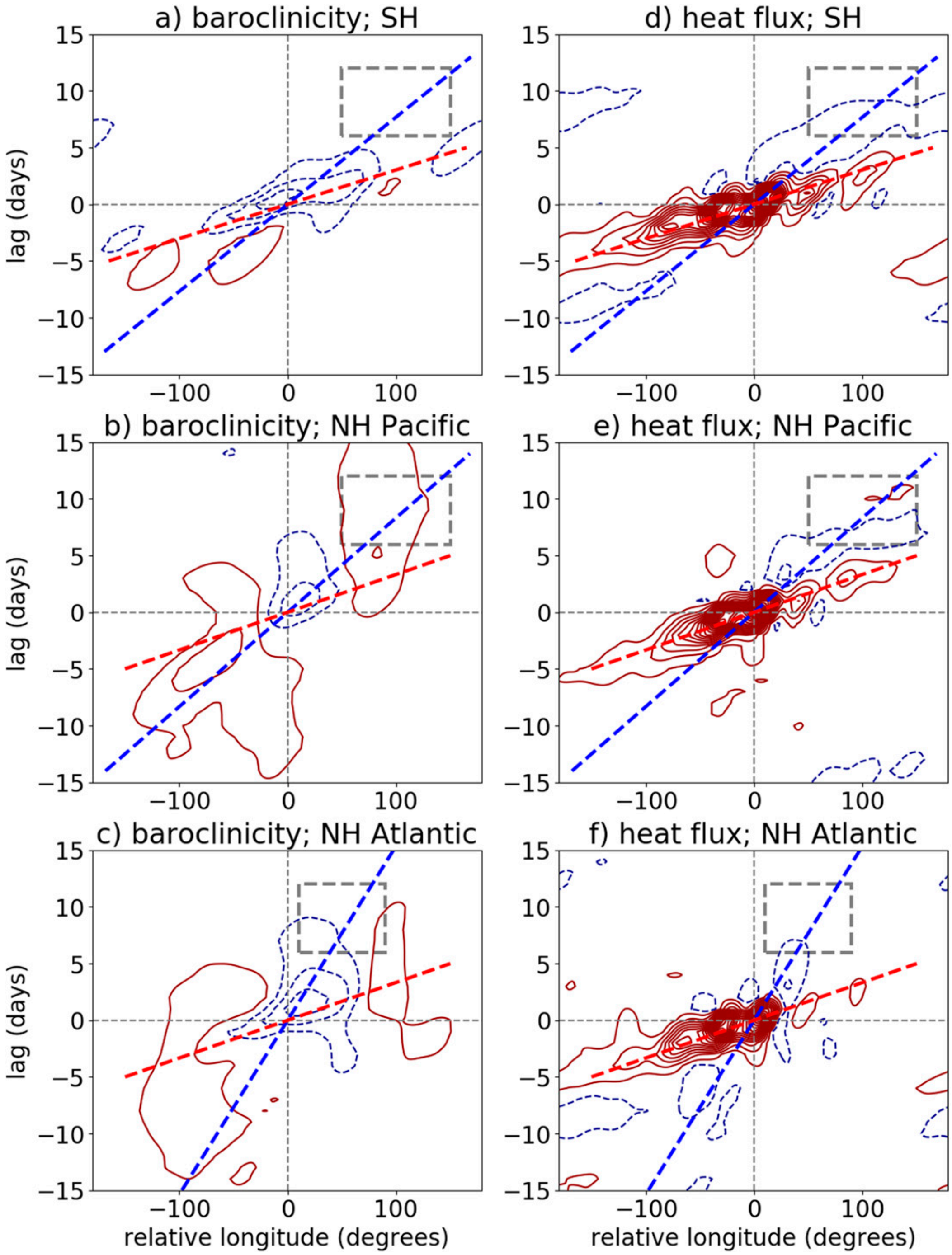

FIG. 6. As in Figs. 1a, 1c, and 1e but for (a)–(c) the baroclinicity at 700 hPa and (d)–(f) the heat flux at 700 hPa (both averaged between 35°–60° latitude) regressed on the same EKE anomaly time series used to construct Fig. 1. Blue and red contours represent negative and positive values, respectively. The values in (a) and (d) were multiplied by −1 so that positive values denote increases in the equator-to-pole temperature gradient and the poleward fluxes of heat in both hemispheres. Blue and red dashed lines as well as gray boxes in each row are the same as in Fig. 1. The contour interval for the baroclinicity is 0.8×10^{-7} K m^{-1} (i.e., . . . , −1.2, −0.4, 0.4, . . . , as in Fig. 5a). The contour interval for the heat fluxes is 0.4 K m s^{-1} (i.e., . . . , −0.6, −0.2, 0.2, . . . , as in Fig. 5b).

zonally confined, such that suppression emerges ~30° to the east of the original disturbance (Fig. 1e).

Downstream suppression may be thought of as a time-varying analog to downstream self-destruction (Kaspi and Schneider 2011a,b). In the case of downstream self-destruction, the self-destroying tendency of baroclinic eddies is hypothesized to constrain the longitudinal extent of the climatological-mean storm tracks. In the case of downstream suppression, it is hypothesized to give rise to out-of-phase variations in eddy activity that emerge to the west of the wave packet as it moves to the east and—importantly—leads to periodic behavior on subseasonal time scales.

As shown in previous work (e.g., TCB17), downstream suppression leads to statistically significant periodicity on time scales of ~20–25 days when EKE is averaged over the SH storm track (Fig. 2a). As shown here, it also leads to periodicity over the North Pacific and North Atlantic storm tracks, although the periodicity is only statistically significant in the Atlantic sector (Fig. 2c) and in the NH zonal mean (Fig. 2d).

The results shown here further reveal that eddy activity in the North Pacific not only seeds North Atlantic storm activity via downstream development on time scales of days (e.g., Chang 1993), but that it also suppresses North Atlantic storm activity on a time scale of a week and more (Figs. 1c and 4). This is potentially important, as it implies that (i) periods of increased eddy activity in the North Pacific are followed by quiescent periods in the North Atlantic, and vice versa, and (ii) the linkages between the North Pacific and North Atlantic storm tracks occur on time scales of up to 10 days and longer. To what extent the suppression of Northern Hemisphere storm track activity contributes to weather prediction on subseasonal time scales remains to be determined.

Acknowledgments. We thank Isaac Held for carefully editing the manuscript, as well as Volkmar Wirth and two anonymous referees for their detailed and constructive reviews of the manuscript. The authors are supported by National Science Foundation Climate and Large-Scale Dynamics program.

Data availability statement. ERA-Interim data were obtained from the European Centre for Medium Range Forecasts website (https://apps.ecmwf.int/datasets/data/interim-full-daily/), and scripts are available upon request.

REFERENCES

Ambaum, M. H. P., and L. Novak, 2014: A nonlinear oscillator describing storm track variability. *Quart. J. Roy. Meteor. Soc.*, **140**, 2680–2684, https://doi.org/10.1002/qj.2352.

Ambrizzi, T., B. J. Hoskins, and H.-H. Hsu, 1995: Rossby wave propagation and teleconnection patterns in the austral winter. *J. Atmos. Sci.*, **52**, 3661–3672, https://doi.org/10.1175/1520-0469(1995)052<3661:RWPATP>2.0.CO;2.

Andrews, D. G., and M. E. McIntyre, 1976: Planetary waves in horizontal and vertical shear: The generalized Eliassen–Palm relation and the mean zonal acceleration. *J. Atmos. Sci.*, **33**, 2031–2048, https://doi.org/10.1175/1520-0469(1976)033<2031:PWIHAV>2.0.CO;2.

Blackmon, M. L., J. M. Wallace, N.-C. Lau, and S. L. Mullen, 1977: An observational study of the Northern Hemisphere wintertime circulation. *J. Atmos. Sci.*, **34**, 1040–1053, https://doi.org/10.1175/1520-0469(1977)034<1040:AOSOTN>2.0.CO;2.

Boljka, L., T. G. Shepherd, and M. Blackburn, 2018: On the coupling between barotropic and baroclinic modes of extratropical atmospheric variability. *J. Atmos. Sci.*, **75**, 1853–1871, https://doi.org/10.1175/JAS-D-17-0370.1.

Bretherton, C. S., M. Widmann, V. P. Dymnikov, J. M. Wallace, and I. Bladé, 1999: The effective number of spatial degrees of freedom of a time-varying field. *J. Climate*, **12**, 1990–2009, https://doi.org/10.1175/1520-0442(1999)012<1990:TENOSD>2.0.CO;2.

Chang, E. K. M., 1993: Downstream development of baroclinic waves as inferred from regression analysis. *J. Atmos. Sci.*, **50**, 2038–2053, https://doi.org/10.1175/1520-0469(1993)050<2038:DDOBWA>2.0.CO;2.

——, 1999: Characteristics of wave packets in the upper troposphere. Part II: Seasonal and hemispheric variations. *J. Atmos. Sci.*, **56**, 1729–1747, https://doi.org/10.1175/1520-0469(1999)056<1729:COWPIT>2.0.CO;2.

——, 2005: The impact of wave packets propagating across Asia on Pacific cyclone development. *Mon. Wea. Rev.*, **133**, 1998–2015, https://doi.org/10.1175/MWR2953.1.

——, and D. B. Yu, 1999: Characteristics of wave packets in the upper troposphere. Part I: Northern Hemisphere winter. *J. Atmos. Sci.*, **56**, 1708–1728, https://doi.org/10.1175/1520-0469(1999)056<1708:COWPIT>2.0.CO;2.

——, S. Lee, and K. L. Swanson, 2002: Storm track dynamics. *J. Climate*, **15**, 2163–2183, https://doi.org/10.1175/1520-0442(2002)015<02163:STD>2.0.CO;2.

Charney, J. G., 1947: The dynamics of long waves in a baroclinic westerly current. *J. Meteor.*, **4**, 136–162, https://doi.org/10.1175/1520-0469(1947)004<0136:TDOLWI>2.0.CO;2.

Dee, D. P., and Coauthors, 2011: The ERA-Interim reanalysis: Configuration and performance of the data assimilation system. *Quart. J. Roy. Meteor. Soc.*, **137**, 553–597, https://doi.org/10.1002/qj.828.

Duchon, C. E., 1979: Lanczos filtering in one and two dimensions. *J. Appl. Meteor.*, **18**, 1016–1022, https://doi.org/10.1175/1520-0450(1979)018<1016:LFIOAT>2.0.CO;2.

Eady, E. T., 1949: Long waves and cyclone waves. *Tellus*, **1**, 33–52, https://doi.org/10.3402/tellusa.v1i3.8507.

Edmon, H. J., B. J. Hoskins, and M. E. McIntyre, 1980: Eliassen–Palm cross sections for the troposphere. *J. Atmos. Sci.*, **37**, 2600–2616, https://doi.org/10.1175/1520-0469(1980)037<2600:EPCSFT>2.0.CO;2.

Gilman, D. L., F. J. Fuglister, and J. M. Mitchell, 1963: On the power spectrum of "red noise." *J. Atmos. Sci.*, **20**, 182–184, https://doi.org/10.1175/1520-0469(1963)020<0182:OTPSON>2.0.CO;2.

Held, I. M., 1975: Momentum transport by quasi-geostrophic eddies. *J. Atmos. Sci.*, **32**, 1494–1497, https://doi.org/10.1175/1520-0469(1975)032<1494:MTBQGE>2.0.CO;2.

Hoskins, B. J., and P. J. Valdes, 1990: On the existence of storm-tracks. *J. Atmos. Sci.*, **47**, 1854–1864, https://doi.org/10.1175/1520-0469(1990)047<1854:OTEOST>2.0.CO;2.

——, and T. Ambrizzi, 1993: Rossby wave propagation on a realistic longitudinally varying flow. *J. Atmos. Sci.*, **50**, 1661–1671, https://doi.org/10.1175/1520-0469(1993)050<1661:RWPOAR>2.0.CO;2.

——, and I. N. James, 2014: *Fluid Dynamics of the Midlatitude Atmosphere*. John Wiley & Sons, 408 pp.

Kaspi, Y., and T. Schneider, 2011a: Downstream self-destruction of storm tracks. *J. Atmos. Sci.*, **68**, 2459–2464, https://doi.org/10.1175/JAS-D-10-05002.1.

——, and ——, 2011b: Winter cold of eastern continental boundaries induced by warm ocean waters. *Nature*, **471**, 621–624, https://doi.org/10.1038/nature09924.

Lau, N.-C., 1979: The structure and energetics of transient disturbances in the Northern Hemisphere wintertime circulation. *J. Atmos. Sci.*, **36**, 982–995, https://doi.org/10.1175/1520-0469(1979)036<1844:OTDOHT>2.0.CO;2.

Lee, S., and I. M. Held, 1993: Baroclinic wave packets in models and observations. *J. Atmos. Sci.*, **50**, 1413–1428, https://doi.org/10.1175/1520-0469(1993)050<1413:BWPIMA>2.0.CO;2.

Lindzen, R. S., and B. Farrell, 1980: A simple approximate result for the maximum growth rate of baroclinic instabilities. *J. Atmos. Sci.*, **37**, 1648–1654, https://doi.org/10.1175/1520-0469(1980)037<1648:ASARFT>2.0.CO;2.

Madden, R. A., and P. R. Julian, 1971: Detection of a 40–50 day oscillation in the zonal wind in the tropical Pacific. *J. Atmos. Sci.*, **28**, 702–708, https://doi.org/10.1175/1520-0469(1971)028<0702:DOADOI>2.0.CO;2.

Novak, L., M. H. P. Ambaum, and R. Tailleux, 2015: The life cycle of the North Atlantic storm track. *J. Atmos. Sci.*, **72**, 821–833, https://doi.org/10.1175/JAS-D-14-0082.1.

Simmons, A. J., and B. J. Hoskins, 1978: The life cycles of some nonlinear baroclinic waves. *J. Atmos. Sci.*, **35**, 414–432, https://doi.org/10.1175/1520-0469(1978)035<0414:TLCOSN>2.0.CO;2.

——, and ——, 1979: The downstream and upstream development of unstable baroclinic waves. *J. Atmos. Sci.*, **36**, 1239–1254, https://doi.org/10.1175/1520-0469(1979)036<1239:TDAUDO>2.0.CO;2.

Stone, P. H., 1978: Baroclinic adjustment. *J. Atmos. Sci.*, **35**, 561–571, https://doi.org/10.1175/1520-0469(1978)035<0561:BA>2.0.CO;2.

Swanson, K., and R. T. Pierrehumbert, 1994: Nonlinear wave packet evolution on a baroclinically unstable jet. *J. Atmos. Sci.*, **51**, 384–396, https://doi.org/10.1175/1520-0469(1994)051<0384:DCCISF>2.0.CO;2.

Thompson, D. W. J., and T. Birner, 2012: On the linkages between the tropospheric isentropic slope and eddy fluxes of heat during Northern Hemisphere winter. *J. Atmos. Sci.*, **69**, 1811–1823, https://doi.org/10.1175/JAS-D-11-0187.1.

——, and E. A. Barnes, 2014: Periodic variability in the large-scale Southern Hemisphere atmospheric circulation. *Science*, **343**, 641–645, https://doi.org/10.1126/science.1247660.

——, and J. D. Woodworth, 2014: Barotropic and baroclinic annular variability in the Southern Hemisphere. *J. Atmos. Sci.*, **71**, 1480–1493, https://doi.org/10.1175/JAS-D-13-0185.1.

——, and Y. Li, 2015: Baroclinic and barotropic annular variability in the Northern Hemisphere. *J. Atmos. Sci.*, **72**, 1117–1136, https://doi.org/10.1175/JAS-D-14-0104.1.

——, B. R. Crow, and E. A. Barnes, 2017: Intraseasonal periodicity in the Southern Hemisphere circulation on regional spatial scales. *J. Atmos. Sci.*, **74**, 865–877, https://doi.org/10.1175/JAS-D-16-0094.1.

Thorncroft, C. D., B. J. Hoskins, and M. E. McIntyre, 1993: Two paradigms of baroclinic-wave life-cycle behaviour. *Quart. J. Roy. Meteor. Soc.*, **119**, 17–55, https://doi.org/10.1002/qj.49711950903.

Vallis, G. K., 2006: *Atmospheric and Oceanic Fluid Dynamics*. Cambridge University Press, 745 pp.

Wang, L., and N. Nakamura, 2015: Covariation of finite-amplitude wave activity and the zonal mean flow in the midlatitude troposphere: 1. Theory and application to the Southern Hemisphere summer. *Geophys. Res. Lett.*, **42**, 8192–8200, https://doi.org/10.1002/2015GL065830.

——, and ——, 2016: Covariation of finite-amplitude wave activity and the zonal-mean flow in the midlatitude troposphere. Part II: Eddy forcing spectra and the periodic behavior in the Southern Hemisphere summer. *J. Atmos. Sci.*, **73**, 4731–4752, https://doi.org/10.1175/JAS-D-16-0091.1.

——, J. Lu, and Z. Kuang, 2018: A robust increase of the intraseasonal periodic behavior of the precipitation and eddy kinetic energy in a warming climate. *Geophys. Res. Lett.*, **45**, 7790–7799, https://doi.org/10.1029/2018GL078495.

Zurita-Gotor, P., 2017: Low-frequency suppression of Southern Hemisphere tropospheric eddy heat flux. *Geophys. Res. Lett.*, **44**, 2007–2015, https://doi.org/10.1002/2016GL072247.